International Journal of Pharmaceutics 433 (2012) 60–70

Contents lists available at SciVerse ScienceDirect

International Journal of Pharmaceutics

journal homepage: www.elsevier.com/locate/ijpharm

A novel image analysis methodology for online monitoring of nucleation and crystal growth during solid state phase transformations

Jian X. Wu[a], Dengning Xia[a,b], Frans van den Berg[c], José Manuel Amigo[c], Thomas Rades[a,d], Mingshi Yang[a], Jukka Rantanen[a,*]

[a] Department of Pharmacy, Faculty of Health and Medical Sciences, University of Copenhagen, Universitetsparken 2, 2100 Copenhagen, Denmark
[b] Department of Pharmaceutics, School of Pharmaceutical Science, Shenyang Pharmaceutical University, Wenhua Road 103, 110016 Shengyang, China
[c] Quality and Technology, Department of Food Science, Faculty of Science, University of Copenhagen, Rolighedsvej 30, 1958 Frederiksberg, Denmark
[d] School of Pharmacy, University of Otago, Dunedin, 9054 Otago, New Zealand

ARTICLE INFO

Article history:
Received 10 February 2012
Received in revised form 26 April 2012
Accepted 27 April 2012
Available online 4 May 2012

Keywords:
Polarized light microscopy
Image analysis
Nucleation
Crystal growth
Solid dispersion
Antisolvent crystallization

ABSTRACT

This study focuses on the development of an automated image analysis method to extract information on nucleation and crystal growth from polarized light micrographs. Using the developed image analysis method, four parameters related to nucleation and crystal growth could be extracted from the images. These parameters were crystalline count (applied as a measure of nucleation), percentage area coverage, average equivalent diameter and average crystalline area (three last parameters applied as a measure for crystal growth). The developed image analysis method was used to investigate two pharmaceutically relevant case studies: first, nitrendipine antisolvent crystallization, and second, recrystallization of amorphous piroxicam solid dispersion in an aqueous environment. In both case studies, an amorphous-to-crystalline phase transformation were observed, which were successfully monitored using real-time Raman spectroscopy. For the both case studies, the parameters related to crystallization kinetics estimated by image analysis were in close agreement with the parameters estimated by Raman spectroscopy. The developed image analysis method proved to be a valuable tool for quantitative monitoring of nucleation and crystal growth with an obvious potential for high throughput screening.

1. Introduction

Characterization of solid state forms is an important part of the drug development process (Newman and Byrn, 2003). It is well known that most active pharmaceutical ingredients (APIs) can exist in a variety of solid state modifications, including both amorphous and various crystalline forms, between which conversions upon processing and storage may occur. Such solid state phase transformations can have a dramatic influence on API morphology, solubility, chemical stability as well as on processability (Heinz et al., 2009; Lee and Myerson, 2006). In solid state research, there is an increased focus on understanding of the amorphous API, due to its increased dissolution rate and solubility as compared to the respective crystalline forms with the potential of increasing bioavailability of many poorly water soluble APIs. However, the main concern related to an amorphous API formulation is the inherent physical instability of amorphous materials due to the increased free energy as compared to its crystalline counterpart (Karmwar et al., 2011), making it susceptible to recrystallization into a more thermodynamically stable form with the consequence of decreased solubility and bioavailability. Monitoring and the subsequent estimation of recrystallization kinetic parameters of solid state phase transformation of an amorphous API into its crystalline counterpart in both, the early development phase as well as the later production stage is thus crucial for the pharmaceutical industry.

Currently, a variety of techniques for monitoring and quantifying solid state phase transformations are available including thermal analytical techniques and spectroscopic techniques (Heinz et al., 2009), such as Raman (Qu et al., 2011; Savolainen et al., 2007), near infrared (NIR) (Zhou et al., 2006), and infrared (IR) spectroscopy (Taylor and Zografi, 1997), as well as wide angle X-ray diffraction (WAXD) (Andronis and Zografi, 2000). A common feature of the thermal analytical techniques is that they allow information related to thermodynamic properties of the sample to be derived, while for the spectroscopic techniques, information related to sample chemistry and molecular interactions can be gained (Reffner et al., 2005). In the solid state phase transformation process such as the amorphous-to-crystalline conversion, it has been shown that nucleation followed by crystal growth are the two important stages (Bhugra and Pikal, 2008). Both, nucleation phase (once the nuclei have reached a certain detectable size) and the following crystal growth can be visualized by the

---

* Corresponding author. Tel.: +45 35336585; fax: +45 35336030.
E-mail address: jtr@farma.ku.dk (J. Rantanen).

0378-5173/$ – see front matter © 2012 Elsevier B.V. All rights reserved.
http://dx.doi.org/10.1016/j.ijpharm.2012.04.074

polarized light microscopy (PLM), allowing kinetic information related to solid state phase transformation to be derived (Andronis and Zografi, 2000).

Despite the potential underlying PLM, much of the studies involving PLM are of a qualitative character. By visually observing polarized light micrographs and by experience-based scoring of the extent of crystallinity, Eerdenbrugh and Taylor estimated the extent of inhibition of crystallization of drugs by different polymers (Van Eerdenbrugh and Taylor, 2010). Using the same scoring system, the authors characterized different APIs in terms of their crystallization rate from amorphous films (Van Eerdenbrugh et al., 2010). In another study by Andronis and Zografi, the authors used PLM to estimate nucleation and crystal growth rate of indomethacin by manually counting the nuclei and measuring the size of crystalline areas of individual polarized light micrographs (Andronis and Zografi, 2000). The above mentioned studies highlight that whilst PLM is a fast and convenient technique in observing nucleation and crystal growth, it is relying on labor intensive consistent counting and measuring of each polarized light micrograph (Andronis and Zografi, 2000). Using PLM and image analysis a study by De Anda et al. showed an example of using high speed camera in qualitative determination of nucleation onset and the presence of different crystal morphologies in batch crystallization (De Anda et al., 2005). An interesting study by Qu et al. demonstrated the ability of video microscopy, in monitoring nucleation and crystal growth in batch crystallization (Qu et al., 2006). However, the authors pointed out that the image analysis routine was complicated with many complex preprocessing steps, due to the complexity in the obtained images such as particulate out of focus problem. Caillet et al. demonstrated the potential of image analysis in online monitoring of crystal size distribution, but noticed that as the solid concentration exceeds a certain limit, their image analysis method gave unrealistic results (Caillet et al., 2007). Not only did these studies demonstrate the value of image analysis in understanding different facets of solid state phase transformation, but also highlight the need to validate the robust region from the image analytical method in which the obtained estimates can be trusted. The present study focuses on the method development and implementation of an automated image analysis routine that allows simultaneous determination of nucleation, crystal growth and overall recrystallization rate of amorphous-to-crystalline phase transformation from polarized light micrographs. The robustness of the developed image analysis routine was initially tested on images generated from computer simulated crystallization. In order to demonstrate the usefulness and broader applicability of the developed image analysis routine, two case studies were then performed.

The first case study is focusing on the determination of nucleation and crystal growth rate of nitrendipine during antisolvent crystallization (Xia et al., 2012), under the influence of increasing polymer concentrations in the aqueous phase. The second case study investigates the nucleation and crystal growth rate of amorphous piroxicam (PRX) formulated as solid dispersion using a solvent evaporation method. The recrystallization rate of PRX from the solid dispersions during a modified dissolution testing is investigated. For both studies, Raman spectroscopy is used as a reference method to follow the amorphous-to-crystalline solid state phase transformations.

2. Methods

2.1. Materials

Nitrendipine was obtained from the Nanjing Pharmaceutical Factory, China. Piroxicam anhydrate (PRX AH) was obtained from Chr. Olesen Pharmaceuticals, Denmark. Polyvinyl alcohol (PVA) with 30–70 kDA molecular weight and 88% alcoholysis was generously supplied by Shin-Etsu Chemical Ind. Co. Ltd., Japan. Polyethylene glycol 200 (PEG) was obtained from Sigma–Aldrich, USA. Polyvinylpyrrolidone (PVP) K90 was obtained from BASF, Germany. Methanol and acetone were obtained from LAB-SCAN analytical sciences, Poland.

2.2. Preparation of nitrendipine and piroxicam references

From earlier studies the nitrendipine supplied by the manufacture was identified as nitrendipine RS-mod. I (Burger et al., 1997; Xia et al., 2012). Amorphous nitrendipine was prepared by dissolving 30 mg/ml nitrendipine in 50% (v/v) PEG 200 and acetone. Two ml of the solution was transferred to 20 ml water kept in an ice-water bath. The precipitated sticky solid body immediately formed is transferred to an aluminum plate and Raman spectra of the sample are recorded.

Piroxicam monohydrate (PRX MH) was prepared in the same way as described in a previous work (Qu et al., 2011). The obtained PRX MH demonstrated identical X-ray powder diffraction pattern as those published in Cambridge Structural Database, CSD (CIDYAP01, Reck et al., 1988).

2.3. Nitrendipine antisolvent crystallization

Nitrendipine was dissolved in a mixture of PEG 200 and 50% (v/v) acetone, and the final drug concentration in the organic solution was 30 mg/ml. PVA was dissolved in aqueous solutions at different concentrations (0.1%, 0.5%, 1% and 2%, w/v), and kept in an ice-water bath. To precipitate the drug, 2 ml of the organic phase containing the drug was transferred to 20 ml of aqueous solution containing PVA under magnetic stirring. All experiments were performed in triplicate.

2.4. Piroxicam solid dispersion crystallization

Five hundred milligrams of PRX:PVP in ratio 1:1 was dissolved in 15 ml acetone and 3.5 ml methanol. 10 μl of solution was pipetted onto a microscope cover glass placed on a hotplate (Krüss G12, Germany) where temperature can be accurately controlled. The temperature on the glass surface was controlled at 30 and 50 °C, and was monitored with a thermo electrode. After complete solvent evaporation, the sample was immediately subjected to a PLM investigation. Samples for Raman spectroscopy were prepared by transferring 40 μl of solution onto an aluminum plate with temperature controlled at 30 and 50 °C on the surface of the plate. All experiments were performed in triplicate.

2.5. Polarized light microscopy

The suspended samples on a glass slide were covered with a 24 mm × 24 mm cover glass, and examined under cross polarized light (Axiolab, Carl Zeiss, Göttingen, Germany) using a 5× magnification and 0.12 numerical aperture objective. Using an attached digital camera (Deltapix, Måløv, Denmark), together with the Deltapix software (ver. 1.6 Deltapix, Måløv, Denmark), a video was captured in uncompressed Audio Video Interleave (AVI) format. Each image frame in the video has 240 ms exposure time and consists of three channels (red, green, blue), each an array of size 1024 × 1280. Particle number density per unit volume was calculated using the depth of field Eq. (1) (Andronis and Zografi, 2000):

$$D_f = \frac{\lambda(1 - NA^2)^{1/2}}{NA^2} \tag{1}$$

where λ and *NA* are the average wavelength of the light used (550 nm) and numerical aperture, respectively.

For the nitrendipine antisolvent crystallization experiments, 40 μl of the suspension prepared as described above was immediately pipetted onto a glass slide and a 4 frames per minute video was captured.

For the modified dissolution testing of PRX solid dispersion, 20 μl of water was pipetted onto the sample, and a video with 12 frames per minute was recorded.

2.6. Image analysis

The raw image data often contains noise in the background, background interference with the regions of interest (crystalline material) and artifacts within the regions of interest. These undesired features necessitate image preprocessing prior to extraction of numerical information from the data. It is outside the scope of this paper to present all the existing image preprocessing techniques since they can be found in e.g., the textbook by Gonzalez and Woods (2008). In this paper, image preprocessing using mathematical morphology on binary images to extract numerical information for quantification purposes was used. Converting the color image into a binary image matrix consisting of elements either 0 or 1, representing black and white pixels respectively, is a simple and convenient method to separate regions of interest (white pixels) from the background (black pixels). However, it was recognized that the binarization process itself can add artifacts, thus necessitating image restoration after binarization (Gonzalez and Woods, 2008). A useful tool in restoring binary images to better reflect the true underlying phenomena is known as mathematical morphology utilizing the mathematical set theory (Gonzalez and Woods, 2008). In the following, the image analysis sequence of each frame in a video will be described using the flow diagram shown in Fig. 1. All frames in the AVI files were analyzed using in-house written script for Matlab (ver. 7.10, Mathworks, U.S.) with the Image Processing Toolbox (ver. 7.10, Mathworks, U.S.) installed. First each image color frame array (raw image), $\boldsymbol{I_{color}}$, with size 1024 × 1280 × 3 (Fig. 2A) was gray scaled by calculating the monochrome luminescence according to Eq. (2) (Buchsbaum, 1975):

$$\boldsymbol{I_{gray}} = 0.2989 \times \boldsymbol{I_{red}} + 0.5870 \times \boldsymbol{I_{green}} + 0.1140 \times \boldsymbol{I_{blue}} \tag{2}$$

where $\boldsymbol{I_{gray}}$, $\boldsymbol{I_{red}}$, $\boldsymbol{I_{green}}$ and $\boldsymbol{I_{blue}}$ are the gray scaled matrix and matrices from the red, green and blue channels, respectively. The elements in the gray scaled matrix span a numerical scale from 0 to 255 (8 bit resolution). Applying a threshold by setting all elements below 25 to 0 and above 25 to 1 in $\boldsymbol{I_{gray}}$, the crystalline objects are separated from the background, and a binary matrix is created (Fig. 2C). At this point the binary image showing one crystalline PRX object (Fig. 2C) contains unfilled regions within the crystalline area. Ideally the counting performed at this stage should result in 1. In practice however, due to the separated pixel regions around the boundary, performing counting at this stage (Fig. 2C) would result in a count of 7.

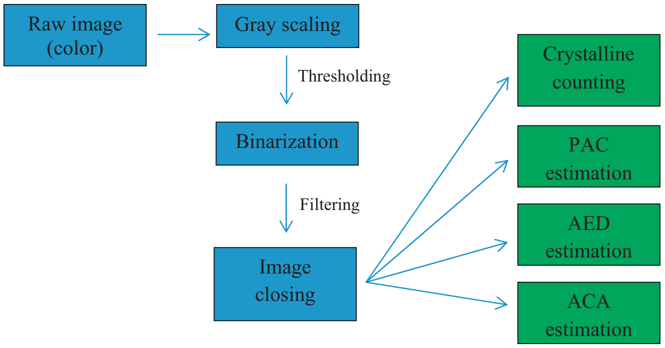

Fig. 1. Image analysis flow diagram showing an overview of the steps in processing of each image frame. The boxes colored in blue are the preprocessing steps, the boxes shown in green are the parameters estimated from each image. Percentage area coverage (PAC), average equivalent diameter (AED) and average crystalline area (ACA). (For interpretation of the references to color in this figure legend, the reader is referred to the web version of the article.)

In order to fill the gaps within the crystal and connect the pixels around the edges, dilation of the binary image $\boldsymbol{I_{bin}}$ with a disk shaped structuring element $\boldsymbol{B}$ (Fig. 2C) is performed using Eq. (3) (Gonzalez and Woods, 2008):

$$\boldsymbol{I_{bin}} \oplus \boldsymbol{B} = \{z|[(\widehat{\boldsymbol{B}})_z \cap \boldsymbol{I_{bin}}] \subseteq \boldsymbol{I_{bin}}\} \tag{3}$$

where z is the set of coordinates in the $\boldsymbol{I_{bin}}$ matrix, and $\widehat{\boldsymbol{B}}$ is the reflection of matrix $\boldsymbol{B}$. The result of the dilation is that holes within the regions of interest that are smaller than the structuring element $\boldsymbol{B}$ get filled up, and the separated pixels around the boundaries are connected to the main crystal. However, the object also grows larger due to the updates of $\boldsymbol{B}$ at the boundaries. In order to restore the original particle size, the dilated matrix $\boldsymbol{I_{bin}}$ is next eroded with the same morphological structuring element $\boldsymbol{B}$ (Fig. 2D) using Eq. (4):

$$\boldsymbol{I_{bin}} \ominus \boldsymbol{B} = \{z|(\boldsymbol{B})_z \subseteq \boldsymbol{I_{bin}}\} \tag{4}$$

When deciding on the shape and size of the morphological structuring element $\boldsymbol{B}$, an important aspect to consider is the distance between two separated particles. If the particle density in the image is high, the small distances between particles can potentially cause a filling of the gap merging the particles together in the dilation step; and it is not possible to separate them again in the subsequent erosion step.

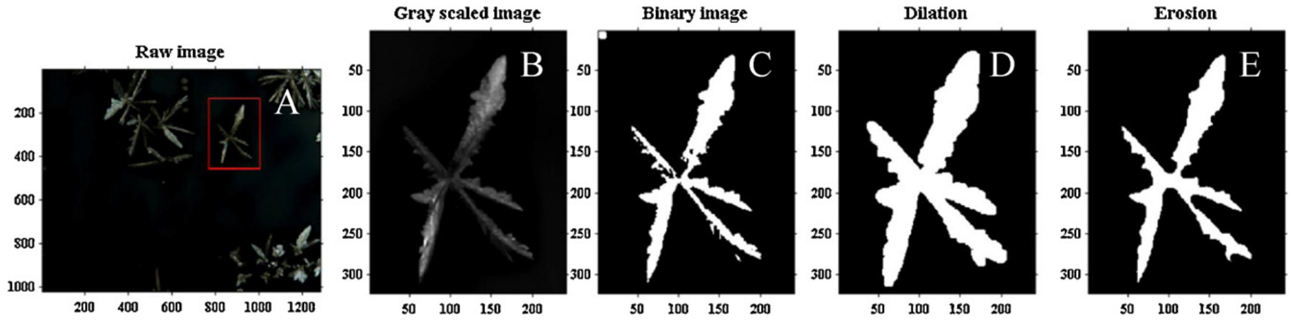

Fig. 2. A sequence of images illustrating the steps in the image preprocessing. A: The original raw color image. B: The gray scaled image of a particle zoomed to the red box of A. C: Binary image obtained by thresholding the gray scaled image B. In the upper left corner a morphological structuring element *B* is shown shaped as a circle with a diameter of 12 pixels. D: Dilation of the binary image C with the morphological structuring element *B*. E: Erosion of the dilated image D with the same morphological structuring element *B*. (For interpretation of the references to color in this figure legend, the reader is referred to the web version of the article.)

The objects in each frame are counted next using the 8-adjacency rule that is in case the center pixel has a value of 1, all 8 pixels surrounding it will also be evaluated, and if one of them has a value of 1, the center pixel will be classified as belonging to that cluster and labeled. The numbers of separated clusters (crystalline count (CC)) after counting is then regarded as the number of crystalline spots in the image. Besides counting, the percentage of white pixels for the entire image is expressed as percentage area coverage (PAC) defined as Eq. (5):

$$\mathrm{PAC} = \frac{A_{sum\ crystalline}}{A_{image}} \times 100\% \tag{5}$$

where $A_{sum\ crystalline}$ and A_{image} are the pixel area of objects from the crystalline material and the total image area respectively. From the definition of PAC in Eq. (5), it is seen that PAC serves as a general parameter in monitoring the overall recrystallization of the sample. In order to monitor and compare crystal growth of different crystal morphology, irrespective of their growth direction, the average equivalent diameter (AED) of a circle computed according to Eq. (6) can be used.

$$\mathrm{AED} = \frac{\sum_{i=1}^{I} \sqrt{4 \times A_i/\pi}}{N} \tag{6}$$

where A_i is the area of the object i, and I is the total number of objects (crystalline spots) in the image, respectively. Using the equivalent diameter as a measure of crystalline size allows description of crystalline growth irrespective of the crystal morphology (Caillet et al., 2007). Another parameter used in monitoring of crystal growth was the average crystalline area (ACA) computed as the average area of crystalline objects in the image. Naturally, several other parameters could be derived from the identified pixel areas, but this would be outside the scope of this article.

2.7. Simulation in assessing robustness of image analysis

In many cases where recrystallization occurs in a solvent medium, the movement of particles is unavoidable. As a consequence multiple objects where boundaries meet or an object below another object will be counted incorrectly as one object. Whenever this occurs, the estimates of CC, PAC, AED and ACA in the polarized light micrograph will be biased as compared to the true values. The extent of this bias will be a function of particle size and the number of particles in the image. In order to get an idea of the robustness of the estimated responses, and to what extent the increase in particle size and number of particles was affecting the predictions of the above mentioned responses, a rudimentary approach by inserting disk shaped structures into a blank image was employed. The routine is written as an in-house Matlab script, where disks of a predefined diameter and number are randomly placed in an array of the same size as the polarized light micrograph image (1024 × 1280). For a given disk size, the maximum number of the disks that can be placed into one image is either 3000 (corresponding to the maximum experimental counted crystalline in one image frame), or estimated from Eq. (7) depending on which of the two values is lowest:

$$N = \frac{I \times J}{d^2} \tag{7}$$

where I, J, d are the number of rows and columns in the image array and disk diameter, respectively. The CC, PAC, AED and ACA are then determined from the array and the accuracy of the response was calculated using a correlation constant k defined in Eq. (8):

$$k = \frac{a_{true}}{a_{pred}} \tag{8}$$

where a_{true} and a_{pred} are the true and predicted response respectively. When k is 1, the predicted and true responses are identical. If the correlation constant is above or below 1, the response is being underestimated or overestimated respectively.

2.8. Raman spectroscopy

Using a wide angle (Phat) probe (Kaiser Optical Systems Inc., Ann Arbor, MI) with a spot size of 3 mm, the samples were monitored online (RamanRxn1 Kaiser Optical Systems, 785 nm Invictus TM NIR diode laser with a standard resolution 9 of 5 cm^{-1} and ~ 100 mW laser power). For nitrendipine antisolvent crystallization experiments, spectra were collected using a 20 s exposure time and 1 accumulation. A total of 40 s was used to obtain each spectrum. For PRX solid dispersion crystallization experiments, spectra were collected using 10 s exposure time and 1 accumulation. A total of 20 s was used to obtain 1 spectrum.

Nitrendipine suspension was prepared as described above. Immediately after the preparation, the suspension was transferred to a 20 °C water bath with magnetic stirring and Raman spectra collected. For the modified dissolution testing of PRX solid dispersions, 80 μl of water was gently dispersed on top of a PRX solid dispersion samples, and Raman spectra collected.

2.9. Multivariate data analysis

Multivariate curve resolution (MCR) was used to analyze the Raman spectra using a Matlab toolbox developed by Jaumot et al. (2005). Mathematically speaking, MCR can be regarded as a bilinear decomposition model, where the data matrix **D** consisting of Raman spectra arranged row-wise with time is decomposed into the concentration matrix **C** and a pure spectral matrix **S** according to Eq. (9):

$$\boldsymbol{D} = \boldsymbol{C}\boldsymbol{S}^T + \boldsymbol{E} \tag{9}$$

where the superscript T means transpose of matrix **S** and **E**, the residual matrix consisting of the part not explained by the model (Jaumot et al., 2005). In order to minimize the problem related to ambiguity from MCR, non-negativity on spectral mode, unimodality on concentration mode and closure constraints were applied to the model for each experiment (de Juan and Tauler, 2006). Evolving factor analysis was used to determine the number of chemical evolving factors for each experiment (Maeder, 1987).

3. Results and discussions

3.1. Response robustness

Evaluation of the robustness of CC, PAC, AED and ACA as a function of particle size and diameter are presented in Fig. 3. In the current study, the maximum counts observed in analyzing the polarized light micrograph frame were below 3000, hence the evaluation of image analysis parameters for their robustness has been up to 3000 or estimated using equation 7 depending on which value is the lowest as previously described. A reliable count estimate was obtained for up to 3000 particles when the particle diameter was below 25 μm, and when particle diameter is above 25 μm, the robustness of CC decreased as a function of particle number (Fig. 3A). Of the four investigated parameters (CC, PAC, AED and ACA), PAC is the most robust parameter since even at high particle diameter and number, the correlation coefficient showed that the true PAC is around 1.4 times higher compared to the estimated PAC (Fig. 3B). The higher robustness of PAC as compared to other parameters can be understood by examining Eq. (5), and imagining a scenario where two or multiple particles overlap each other. Because the pixel area of the entire image array is much higher as compared to the overlapped pixel area, the error caused by under

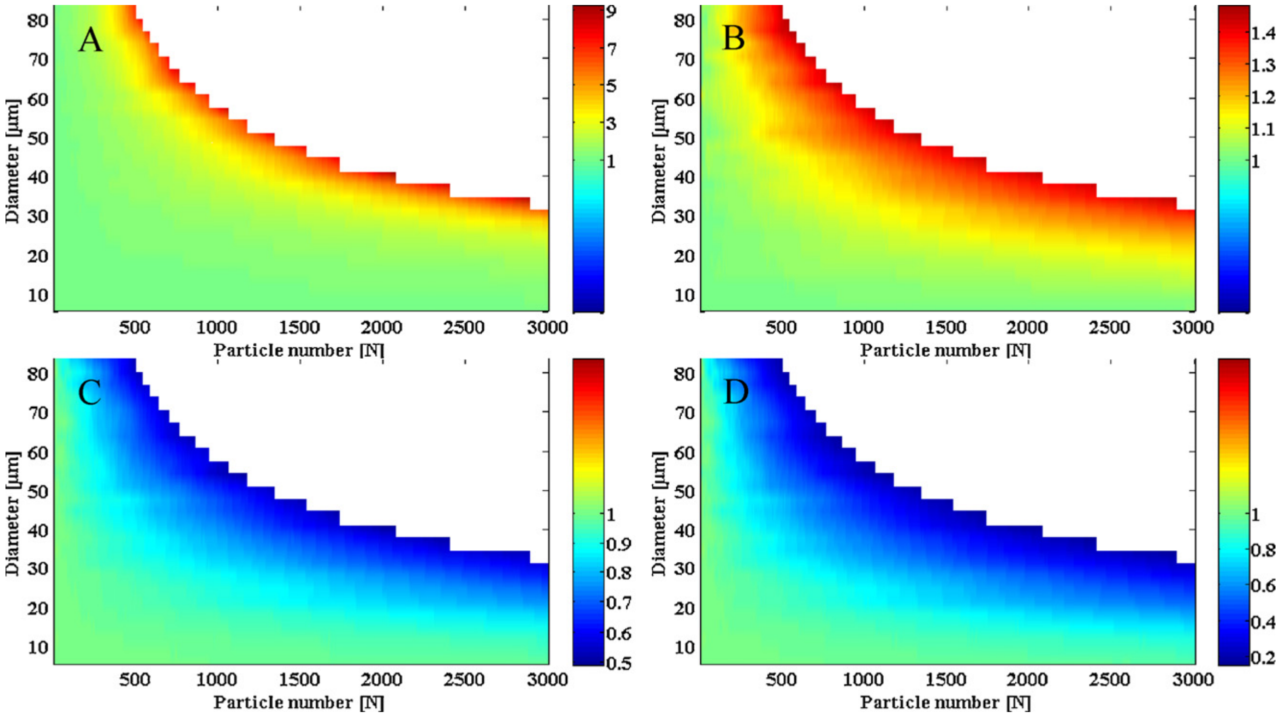

Fig. 3. Robustness of responses as a function of particle diameter and number. The response surfaces represent the correlation coefficient *k*. A: Crystalline count (CC), B: percentage area coverage (PAC), C: average equivalent diameter (AED), D: average crystalline area (ACA). The white area in each response plot was not investigated because it is unrealistic that particles with the given size and count can be contained within the entire image array.

prediction of PAC will be low. In contrast to CC and PAC, an increase in particle diameter and count leads to over estimation of AED and ACA (Fig. 3C and D). It should be noted that AED is more robust as compared to ACA, since the region where *k* is around 1 is larger for AED as compared to ACA. The reason behind this finding is due to the squared relation between disk shaped particle area and its radius. Hence, once disk shaped particles merged together, a relatively small increase in diameter would lead to a relatively larger increase in area. From the above discussions, it is concluded that counting at increased particle number and diameter is the most unstable response. In contrast even though bias exists for AED and ACA at the same region, due to the fact that AED and ACA are calculated as a mean value, the bias is smaller as compared to the counting response.

3.2. Nitrendipine antisolvent crystallization

3.2.1. Original polarized light micrographs

An example of unprocessed images from nitrendipine antisolvent crystallization with 0.1% PVA obtained at successive time points is presented in Fig. 4. These examples highlight that both the number of crystalline counts as well as the overall size of crystalline nitrendipine are increasing as a function of time. In order to obtain parameters that empirically describe nucleation and crystal growth rate it is necessary to extract numerical information from Fig. 4. From an image analysis point of view, and as discussed under Section 2.6, the ability to estimate the rates related to nucleation and growth of crystals relies on isolation of each cluster in the image, and estimation of the number of pixels that each cluster is composed of.

3.2.2. Estimation of nucleation and crystal growth

Nucleation and crystal growth profiles for nitrendipine antisolvent crystallization experiments are presented in Fig. 5. When both AED and ACA are used as responses for crystal growth, it can be observed from Fig. 5C and D that the initial profile significantly deviates from the fitted curve. This deviation can be attributed to the heterogeneous nucleation on particles which are unavoidably present during the experiments. At this stage, with only a few particles present, the presence of large nuclei led to overestimation of the true average size of crystals. However, as time proceeds, more nuclei are formed, less weight is given to the outliers on the estimation of true average crystal size.

From Fig. 5, it is evident that the phase of nucleation and crystal growth of nitrendipine from aqueous phase containing 0.1–0.5% PVA is separated. The nucleation phase ends at around 2 and 4 min

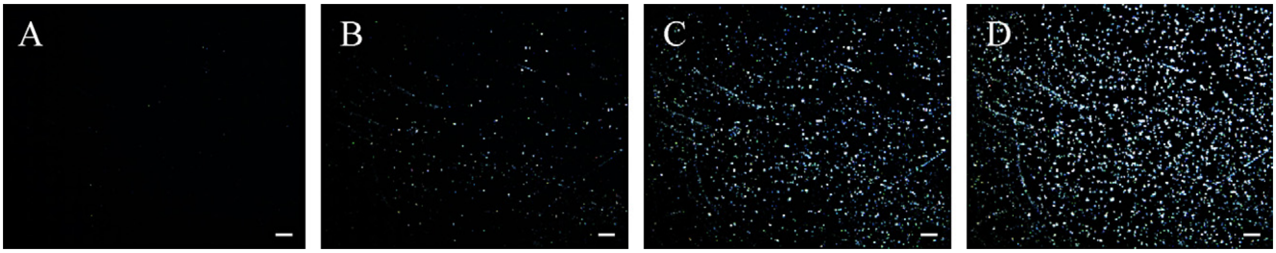

Fig. 4. Polarized light micrograph at increasing time showing nitrendipine antisolvent crystallization from aqueous phase containing 0.1% PVA. A, B, C, D corresponds to frames at 1, 2, 3 and 4 min, respectively. The scale bar corresponds to 100 µm.

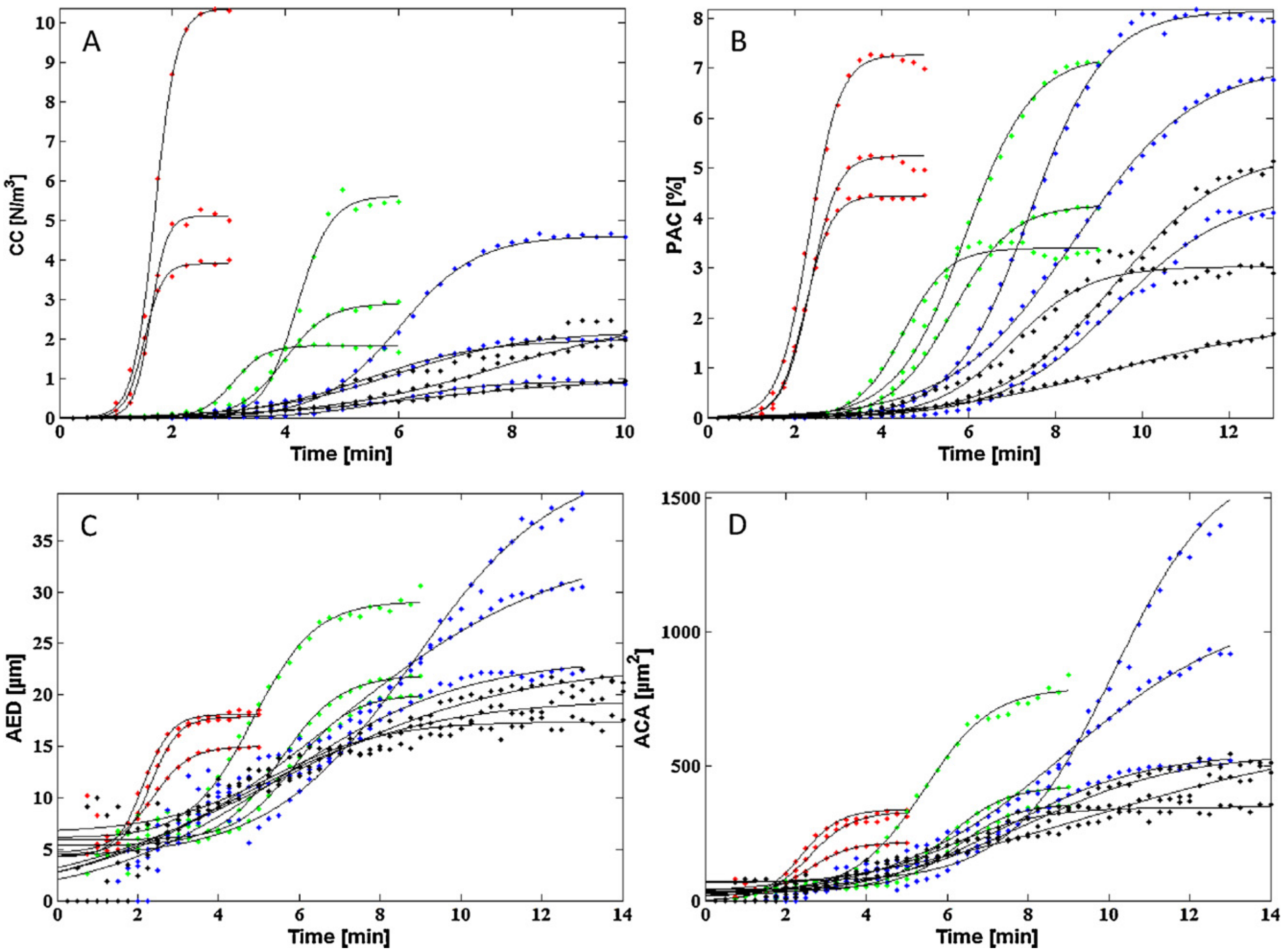

Fig. 5. Nucleation and crystal growth profiles for the nitrendipine antisolvent crystallization experiment with an increase in PVA concentration in the aqueous phase. A: Nucleation profile based on crystalline count (CC). B: Percentage area coverage (PAC) profile. C: Average equivalent diameter (AED) profile. D: Average crystalline area (ACA) profile. Red, green, blue and black corresponds to 0.1, 0.5, 1 and 2% PVA in the aqueous phase, respectively ($n = 3$ at each concentration of PVA). (For interpretation of the references to color in this figure legend, the reader is referred to the web version of the article.)

(Fig. 5A), while the crystal growth phase starts to dominate from 2 to 4 min and onwards, respectively (Fig. 5B–D). However, when the concentration of PVA in aqueous phase exceeds 0.5%, the nucleation and crystal growth phases are no longer separated. It indicates that a PVA concentration above 1% has an insignificant inhibition effect on nucleation.

The profiles from nucleation and crystal growth follow a sigmoidal shape (Fig. 5), hence the empirical nucleation and crystal growth rates can be derived from the β constant, obtained by fitting the profiles to equation 10 (Qu et al., 2011; Wikström et al., 2009):

$$X = X_0 + \frac{\alpha}{1 + \exp(-\beta \times (t - t_{50}))} \tag{10}$$

where X_0, α and t_{50} are the initial level offset of the response, equilibrated response and the time needed to reach 50% toward the equilibrated state, respectively. The β and t_{50} estimated by fitting the transformation profiles shown in Fig. 5 to Eq. (10) is plotted against their respective PVA concentration (Fig. 6). As can be seen from Fig. 6, increasing the PVA concentration in the aqueous phase from 0.1 to 1% has a significant effect on decreasing the β constant for both responses related to nucleation as well as crystal growth. It is also evident from Fig. 6 that the β constant of nucleation and crystal growth was not significantly decreased with an increase in PVA concentration above 1% in the aqueous phase. The same trend is seen for the t_{50} value, since an increase in PVA concentration above 1% did not significantly increase the t_{50} value as compared to increasing PVA concentration between 0.1 and 1% (Fig. 6). Fig. 6A also presents the particle AED span when solid state phase transformation has reached an equilibrium. A lower solid state transformation rate (low β constant) was observed when the particle size distribution (span) was higher and vice versa. A higher nucleation rate can generate crystals with smaller particle size, which is due to the higher density of nuclei in the sample. The high density of nuclei can also lead to a fast consumption of the dissolved supersaturated nitrendipine in the surrounding of each nucleus. Ultimately, the outcome is the formation of many particles with a narrow particle size distribution (Sugimoto, 2007).

3.2.3. *Raman monitoring of nitrendipine antisolvent crystallization*

Raman spectra for nitrendipine crystalline reference, amorphous nitrendipine and the monitored nitrendipine amorphous-to-crystalline transformation are shown in Fig. 7A. The characteristic Raman band of raw crystalline nitrendipine was observed at 1120, 1213, 1347, 1645 cm^{-1}, which have been assigned to pyridine in plane vibration, C—O—C vibration, symmetric NO$_2$ stretch and C═C stretch respectively (Socrates, 2004; Tang et al., 2002). From Fig. 7A, in agreement with other studies (Chieng et al., 2009; Savolainen et al., 2007), it can be observed that the main difference between amorphous and crystalline nitrendipine is the lower intensity and band broadening of the amorphous form due to the

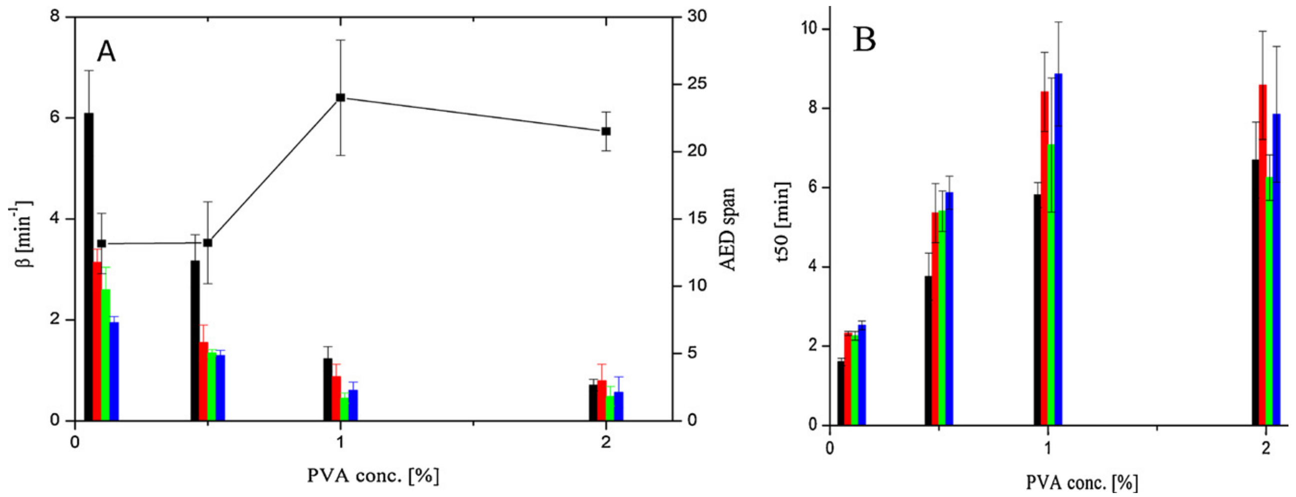

Fig. 6. Fitted β and t_{50} values from nucleation and crystal growth profiles for the nitrendipine antisolvent crystallization experiment with an increase in PVA concentration in the aqueous phase ($n = 3$). A: bar plot showing the fitted β values of crystalline count (CC), percentage area coverage (PAC), average equivalent diameter (AED), average crystalline area (ACA) as black, red, green and blue bars, respectively. The connected black squares indicate the equivalent average diameter (AED) span. B: bar plot of the fitted t_{50} values. The color sequence of the bars is the same as mentioned for A. (For interpretation of the references to color in this figure legend, the reader is referred to the web version of the article.)

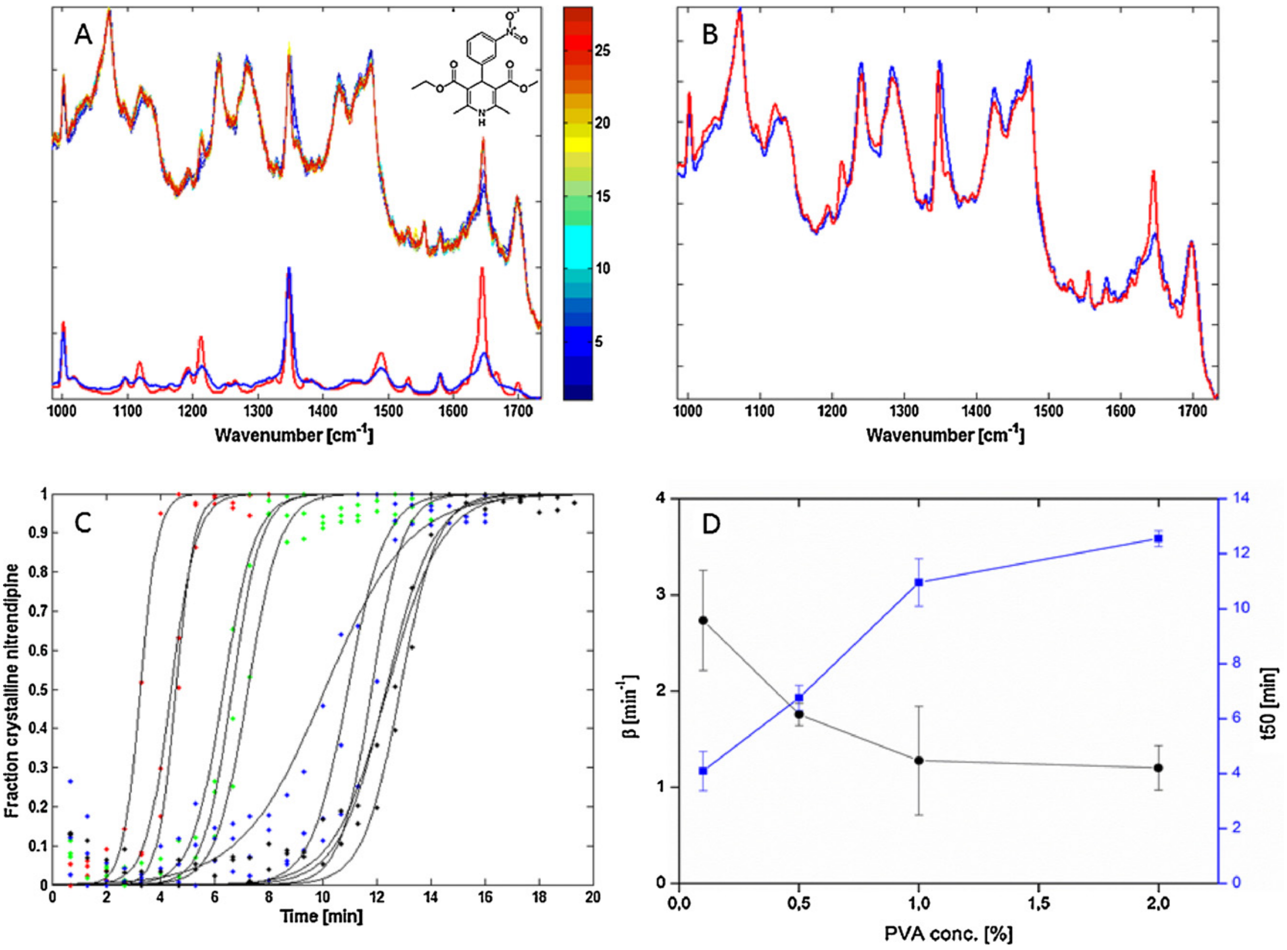

Fig. 7. Example of a MCR model on nitrendipine antisolvent crystallization in the presence of 0.1% PVA in aqueous phase. A: (Top right-hand side) Nitrendipine molecular structure. (Top spectra) The colored SNV corrected Raman spectra obtained during real-time monitoring of nitrendipine antisolvent crystallization. The color indicates time, spectra are arranged according to acquisition order (see color bar on the right). (Bottom spectra) Separate spectra in the lower part of the figure correspond to reference spectra obtained with raw crystalline nitrendipine (red) and amorphous nitrendipine (blue). B: Pure spectra obtained after MCR. Blue and red spectra model amorphous and crystalline nitrendipine, respectively. C: Nitrendipine antisolvent crystallization experiments with 0.1, 0.5, 1 and 2% PVA concentration in the aqueous phase indicated with red, green, blue and black data points respectively. The curves are fitted according to equation 10 ($n = 3$). D: Fitted t_{50} (blue) and β (black) from conversion profiles in C ($n = 3$). (For interpretation of the references to color in this figure legend, the reader is referred to the web version of the article.)

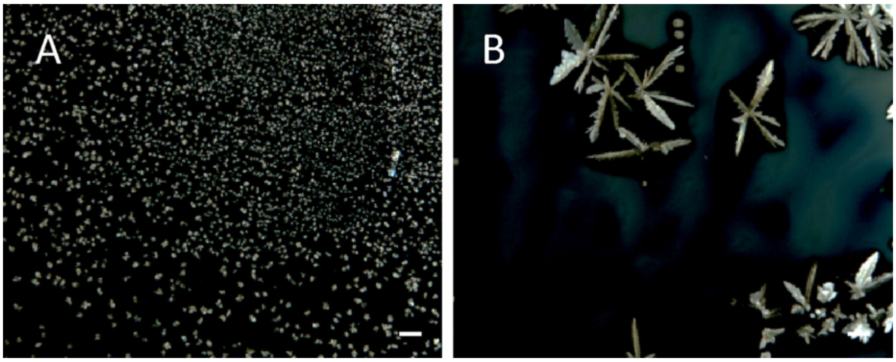

Fig. 8. Polarized light micrographs of equilibrated samples evaporated at A: 30 °C and B: 50 °C. The scale bar corresponds to 100 μm.

lack of long range molecular order. It is evident from the transformation spectra in Fig. 7A that other Raman bands related to excipients and acetone are also present, however, it is worthy to note from Fig. 7B that the major differences in the two modeled pure spectra are due to amorphous and crystalline nitrendipine. It suggests that the influence from excipients is removed in the final model. Evolving factor analysis revealed two significant evolving components (data not shown), which is most likely attributed to the evolution of amorphous and crystalline nitrendipine components during the solid state phase transformation. Fig. 7C is presenting the conversion profiles with the fitted β and t_{50} parameters shown in Fig, 7D. The β value determined from Raman monitoring (Fig. 7D) is in close agreement with the β value from the polarized light microscopy experiment when PAC, AED and ACA are used as responses (Fig. 6). Comparing fitted t_{50} values from the Raman measurements with the t_{50} values from image analysis, it can be seen that the t_{50} values from Raman are higher as compared to the t_{50} values from the image analysis. It can be concluded that in this case, the anti-solvent crystallization experiments performed under polarized light microscopy closely resembled the bulk anti-solvent conversion experiments when monitored with Raman spectroscopy in terms of conversion rate.

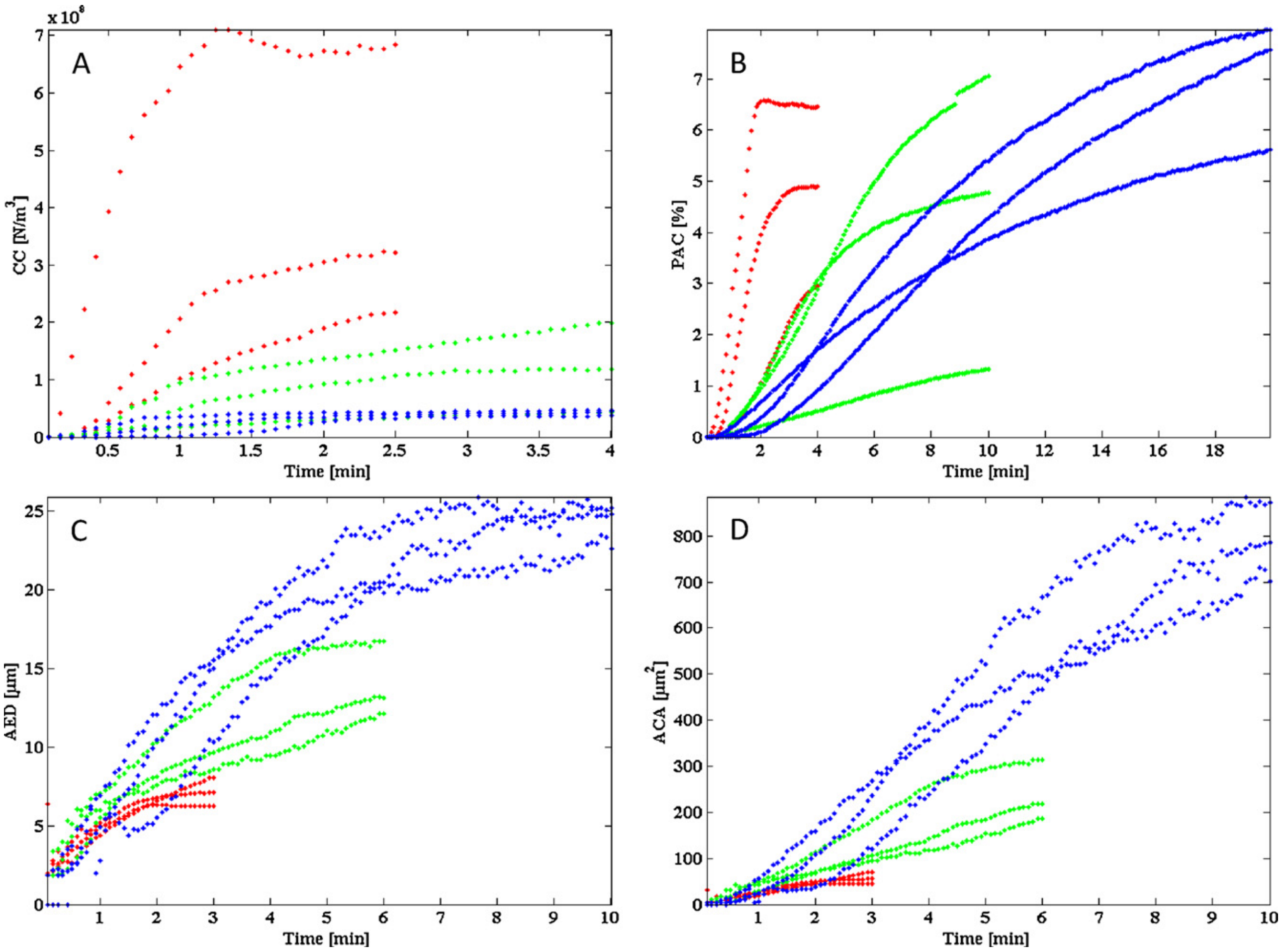

Fig. 9. Nucleation and crystal growth profiles of PRX solid dispersion crystallization in aqueous environment. A: Nucleation profile based on crystalline count (CC), B: percentage area coverage (PAC), C: average equivalent diameter (AED), and D: average crystalline area (ACA). Red, green and blue belongs to samples evaporated at 30, 40 and 50 °C, respectively ($n = 3$). (For interpretation of the references to color in this figure legend, the reader is referred to the web version of the article.)

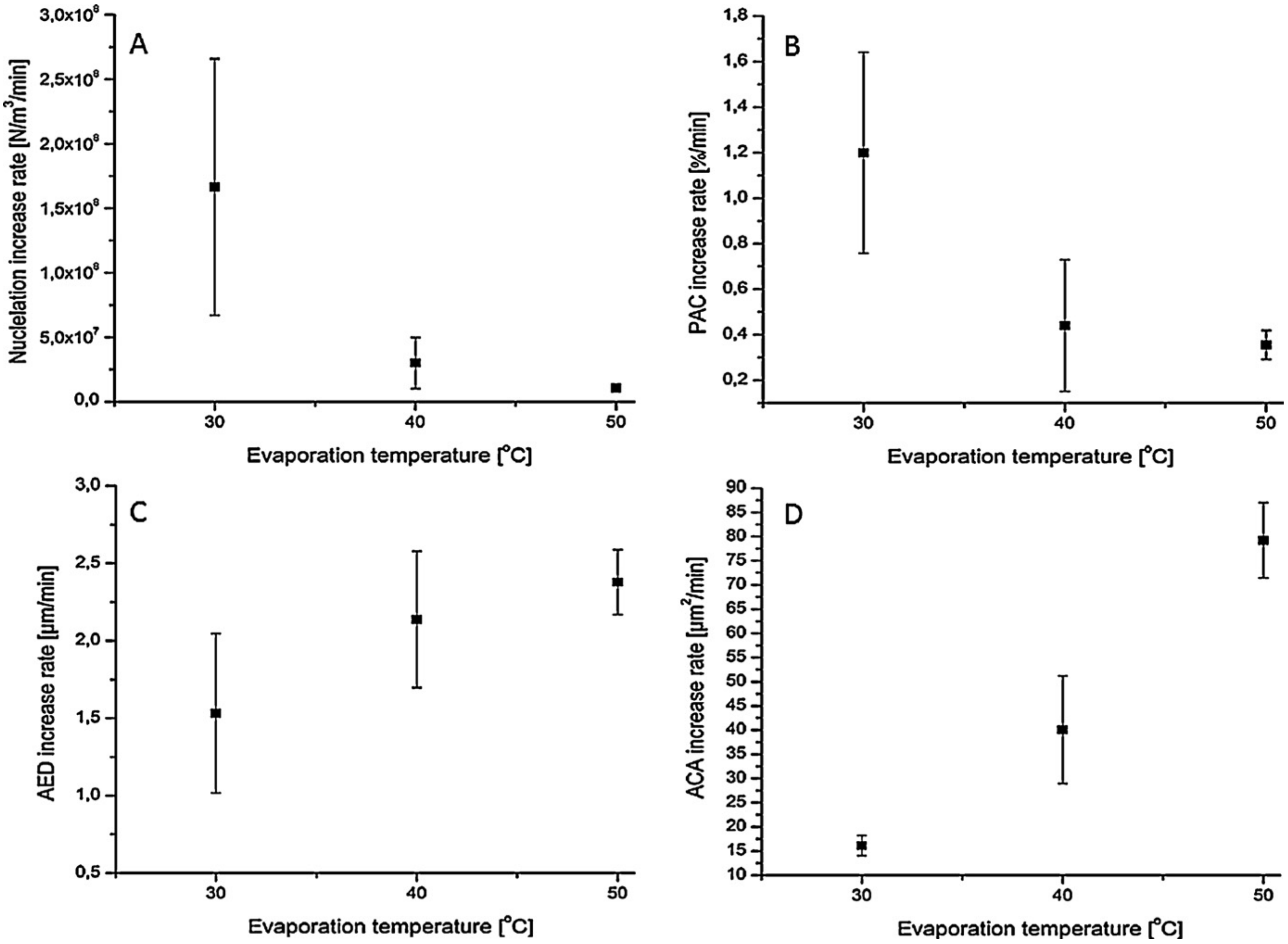

Fig. 10. Absolute average nucleation and crystal growth rates ($n = 3$). A: nucleation, B: percentage area coverage (PAC), C: average equivalent diameter (AED) and D: average crystalline area (ACA).

However, since the volume of the bulk where anti-solvent crystallization takes place is much larger as compared to the volume between the two glass plates from the polarized light microscope experiments, a delay in the bulk crystallization as compared to the crystallization under polarized light microscopy is manifested in higher t_{50} values.

3.3. Modified piroxicam solid dispersion dissolution experiment

3.3.1. Piroxicam solid dispersion crystallization

Polarized light micrographs of equilibrated PRX crystals in solid dispersions prepared at 30 and 50 °C evaporation temperature are presented in Fig. 8. Evaporation at low temperature (30 °C) increased the density of nuclei when compared with the high solvent evaporation temperature (50 °C). The blue opalescence region between crystals (Fig. 8B) can be observed only with samples prepared using 50 °C evaporation temperature. The solid state nature of the submicron bodies responsible for the blue opalescence is not fully understood. Prenucleation events and related molecular clustering prior to nucleation has been discussed in the literature (Lee and Myerson, 2006). An alternative theory to the classical nucleation theory has been suggested, in which molecular clusters, metastable with respect to the crystalline state, are created from the supersaturated liquid. This event is subsequently followed by ordering into the crystalline state (Lee and Myerson, 2006). This theory may be used in explaining the blue shaded, opalescent regions in Fig. 8B.

In agreement with visual observation of the polarized light microscope images (Fig. 8), an increase in solvent evaporation temperature decreased the density of nuclei when equilibrium has been reached (Fig. 9A). The nucleation rate was increased when samples were prepared using a low solvent evaporation temperature (30 °C) as compared to a high solvent evaporation temperature (50 °C) (Fig. 10A). This finding suggests that solid dispersion samples prepared using a low solvent evaporation temperature (30 °C) may contain molecular cluster regions in the amorphous phase. Upon contact with water, these regions act as nucleation sites leading to a higher number of nuclei. Because the initial nucleation rate is higher for samples prepared at 30 °C compared to those at 50 °C evaporation temperature, the degree of PRX supersaturation must be lower with the 30 °C samples immediately after the nucleation phase. Hence, it is likely that the molecular clusters can also act as reservoir in replenishing the consumed PRX for solid dispersions prepared at 50 °C solvent evaporation temperature. Ultimately, this leads to a longer recrystallization time as manifested in Fig. 9B, and increased crystal growth rate when solvent evaporation temperature is increased (Figs. 9C and D and 10C and D).

The change in nucleation and crystal growth profiles and corresponding rates as a function of solvent evaporation temperature confirms the statement from Leuner and Dressman (2000) that a variation in solvent evaporation temperature can have great implications on product performance. Several authors have shown that an increase of PVP:drug ratio in solid dispersion increases the drug dissolution rate (Kearney et al., 1994; Tantishaiyakul et al.,

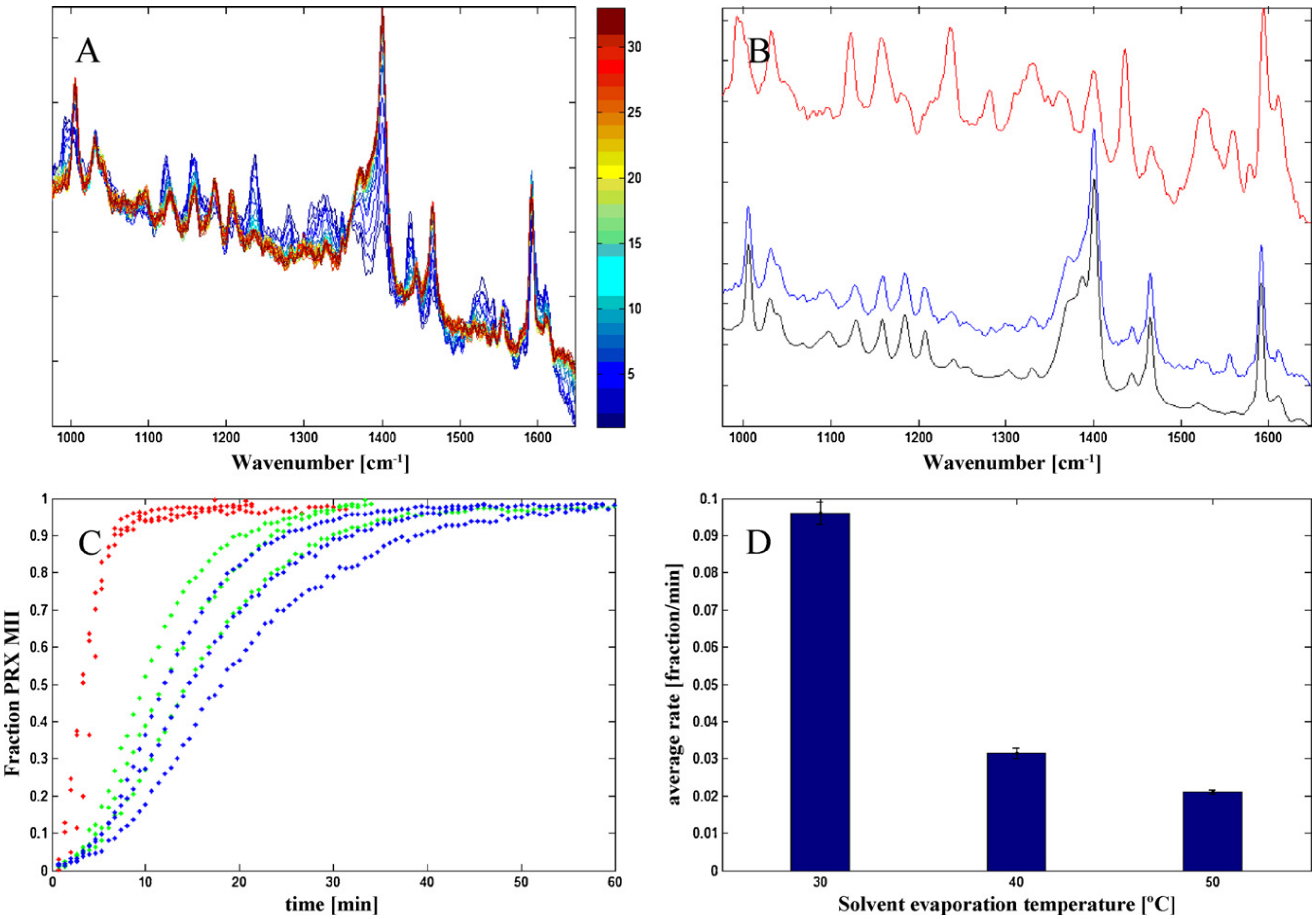

Fig. 11. MCR model based on Raman monitoring of solvent mediated PRX crystallization. A: An example of SNV corrected Raman conversion data of PRX solid dispersion evaporated at 30 °C. The color indicates time, spectra are arranged according to acquisition order (see color bar to right). B: Pure calculated amorphous PRX, pure calculated PRX monohydrate and reference PRX monohydrate Raman spectra shown in red, blue and black, respectively. C: PRX amorphous-to-crystalline solvent mediated conversion profiles of solid dispersions prepared at 30, 40, 50 °C shown as red, green and blue plot, respectively ($n = 3$). D: Average conversion rate calculated on the basis of conversion profiles in C ($n = 3$). (For interpretation of the references to color in this figure legend, the reader is referred to the web version of the article.)

1999). Many reasons have been suggested for this finding, such as increased wettability due to PVP, reduction of the drug particle size to an absolute minimum within solid dispersion (Vasconcelos et al., 2007) and the presence of different solid state forms of the drug within the polymer matrix (Tantishaiyakul et al., 1999). Findings from the present study highlight that in addition to dissolution rate being affected by the factors mentioned, it may also be affected by the kinetics of recrystallization of the amorphous drug within the polymer matrix upon contact with the dissolution medium. A study from Brouwers et al. highlights the importance of stabilization of supersaturation by excipients in order to inhibit or delay drug precipitation (Brouwers et al., 2009). From this perspective, the method for quantification of nucleation and crystal growth proposed in this study, has the potential of screening the stabilizing effect of excipients on supersaturated drug solution upon solid dispersions dissolution testing.

3.3.2. *Raman monitoring of piroxicam solid dispersion conversion*

Evolving factor analysis performed on each Raman PRX crystallization data set revealed 2 significant factors, suggesting the change in two components, i.e., amorphous and crystalline PRX. The Raman spectrum obtained initially from the solvent mediated PRX solid dispersion conversion revealed broader and lower intensity bands as compared to the final Raman spectrum (shown as dark blue and red spectra in Fig. 11A, respectively). This finding suggests more amorphous PRX being present initially as compared to the later phase of conversion (Savolainen et al., 2007). The pure spectrum obtained from the MCR model of amorphous PRX is in good agreement with the experimental spectrum reported by Kogermann et al. (2011), and the pure spectrum of crystalline PRX matched with the experimental spectrum of PRX monohydrate (Fig. 11B). Since only two evolving factor components were identified in the data set (amorphous and crystalline PRX), it can be concluded that the solid state phase transformation for amorphous PRX in solid dispersion is a single step transformation in aqueous environment. A previous study investigating the physical stability of the same PRX solid dispersion formulation stored at 53% RH and 25 °C revealed that the solid state phase transformation of amorphous PRX was following the Ostwald's step rule yielding, first, the unstable PRX AH form II (Vrecer et al., 2003) and second, the formation of the more stable PRX AH form I (Wu et al., 2011). These findings suggest that different mechanisms are responsible for the recrystallization of amorphous PRX solid dispersion in aqueous environment.

Amorphous-to-crystalline conversion profiles (Fig. 11C) and the calculated average conversion rates (Fig. 11D) clearly indicate a decrease in the conversion rate as solvent evaporation temperature is increased. It has been shown that an increase in solvent evaporation rate has a negative effect on the crystallization of PRX in solid dispersion (Wu et al., 2011). The most likely explanation behind this finding is that a rapid evaporation of solvent decreases the possibility for PRX molecules to rearrange into molecular clusters in the amorphous phase upon precipitation. Upon contact with water, the formulation prepared using low solvent evaporation temperature (30 °C) has a faster nucleation rate (Fig. 10A), leading to an overall faster amorphous-to-crystalline solid state transformation (Figs. 10B and 11D).

Comparing solid state phase transformation rates of PRX recrystallization monitored with image analysis and Raman spectroscopy, it can be concluded that Raman spectroscopy has the particular advantage being capable of monitoring the overall evolution of solid state phase transformation together with identification of the polymorphic forms. In contrast, the image analysis approach is particularly useful in obtaining knowledge related to the nucleation and crystal growth kinetics.

4. Conclusion

The image analysis routine established in the current study represents a relatively easy and convenient way in obtaining quantitative information on various aspects of crystallization, with the estimated kinetic values in close agreement with the values found from real-time Raman monitoring. In comparing the four image analysis responses (CC, PAC, AED and ACA), PAC and CC were found to be the most and least robust response, respectively.

Using the developed image analysis technique the following two specific conclusions could be drawn. First, for the nitrendipine anti-solvent crystallization, an increase in PVA concentration from 0.1 to 1% significantly decreased nucleation and crystal growth rate of nitrendipine. Second, for the modified PRX solid dispersion dissolution testing, an increase in solvent evaporation rate upon solid dispersion preparation decreased the nucleation rate but increased the crystal growth rate in the following modified dissolution testing in aqueous environment.

Acknowledgements

JXW, MY and JR gratefully acknowledge funding from the Danish Council of Technology and Innovation for the Innovation Consortium NanoMorph (952320/2009). M.Y. also acknowledges the starting grant of associate professor from Faculty of Medical and Health Sciences, University of Copenhagen.

References

Andronis, V., Zografi, G., 2000. Crystal nucleation and growth of indomethacin polymorphs from the amorphous state. J. Non-Cryst. Solids 271, 236–248.

Bhugra, C., Pikal, M.J., 2008. Role of thermodynamic, molecular, and kinetic factors in crystallization from the amorphous state. J. Pharm. Sci. 97, 1329–1349.

Brouwers, J., Brewster, M.E., Augustijns, P., 2009. Supersaturating drug delivery systems: the answer to solubility-limited oral bioavailability? J. Pharm. Sci. 98, 2549–2572.

Buchsbaum, W.H., 1975. Color TV Servicing, 3rd ed. Prentice-Hall, Englewood Cliffs.

Burger, A., Rollinger, J.M., Brüggeller, P., 1997. Binary system of (R)- and (S)-nitrendipine—polymorphism and structure. J. Pharm. Sci. 86, 674–679.

Caillet, A., Rivoire, A., Galvan, J.-M., Puel, F., Fevotte, G., 2007. Crystallization of monohydrate citric acid. 1. In situ monitoring through the joint use of Raman spectroscopy and image analysis. Cryst. Growth Des. 7, 2080–2087.

Chieng, N., Rehder, S., Saville, D., Rades, T., Aaltonen, J., 2009. Quantitative solid-state analysis of three solid forms of ranitidine hydrochloride in ternary mixtures using Raman spectroscopy and X-ray powder diffraction. J. Pharm. Biomed. Anal. 49, 18–25.

De Anda, J.C., Wang, X.Z., Lai, X., Roberts, K.J., Jennings, K.H., Wilkinson, M.J., Watson, D., Roberts, D., 2005. Real-time product morphology monitoring in crystallization using imaging technique. AIChE J. 51, 1406–1414.

de Juan, A., Tauler, R., 2006. Multivariate curve resolution (MCR) from 2000: progress in concepts and applications. Crit. Rev. Anal. Chem. 36, 163–176.

Gonzalez, R.C., Woods, R.E., 2008. Digital Image Processing, 3rd ed. Prentice Hall, Upper Saddle River, NJ.

Heinz, A., Strachan, C.J., Gordon, K.C., Rades, T., 2009. Analysis of solid-state transformations of pharmaceutical compounds using vibrational spectroscopy. J. Pharm. Pharmacol. 61, 971–988.

Jaumot, J., Gargallo, R., de Juan, A., Tauler, R., 2005. A graphical user-friendly interface for MCR-ALS: a new tool for multivariate curve resolution in MATLAB. Chemom. Intell. Lab. Syst. 76, 101–110.

Karmwar, P., Graeser, K., Gordon, K.C., Strachan, C.J., Rades, T., 2011. Investigation of properties and recrystallisation behaviour of amorphous indomethacin samples prepared by different methods. Int. J. Pharm. 417, 94–100.

Kearney, A.S., Gabriel, D.L., Mehta, S.C., Radebaugh, G.W., 1994. Effect of polyvinylpyrrolidone on the crystallinity and dissolution rate of solid dispersions of the antiinflammatory CI-987. Int. J. Pharm. 104, 169–174.

Kogermann, K., Veski, P., Rantanen, J., Naelapää, K., 2011. X-ray powder diffractometry in combination with principal component analysis—a tool for monitoring solid state changes. Eur. J. Pharm. Sci. 43, 278–289.

Lee, A.Y., Myerson, A.S., 2006. Particle engineering: fundamentals of particle formation and crystal growth. MRS Bull. 31, 881–886.

Leuner, C., Dressman, J., 2000. Improving drug solubility for oral delivery using solid dispersions. Eur. J. Pharm. Biopharm. 50, 47–60.

Maeder, M., 1987. Evolving factor analysis for the resolution of overlapping chromatographic peaks. Anal. Chem. 59, 527–530.

Newman, A.W., Byrn, S.R., 2003. Solid-state analysis of the active pharmaceutical ingredient in drug products. Drug Discov. Today 8, 898–905.

Qu, H., Louhi-Kultanen, M., Kallas, J., 2006. In-line image analysis on the effects of additives in batch cooling crystallization. J. Cryst. Growth 289, 286–294.

Qu, H., Munk, T., Cornett, C., Wu, J.X., Bøtker, J., Christensen, L., Rantanen, J., Tian, F., 2011. Influence of temperature on solvent-mediated anhydrate-to-hydrate transformation kinetics. Pharm. Res. 28, 364–373.

Reck, G., Dietz, G., Laban, G., Gunther, W., Bannier, G., Hohne, E., 1988. X-ray studies on piroxicam modifications. Pharmazie 43, 477–481.

Reffner, J.A., Seelenbinder, J.A., Norman, M.L., 2005. Integrating polarized light microscopy with vibrational spectroscopy for solid-state characterization of drug substances. Microsc. Microanal. 11, 1234–1235.

Savolainen, M., Heinz, A., Strachan, C., Gordon, K.C., Yliruusi, J., Rades, T., Sandler, N., 2007. Screening for differences in the amorphous state of indomethacin using multivariate visualization. Eur. J. Pharm. Sci. 30, 113–123.

Socrates, G., 2004. Infrared and Raman Characteristic Group Frequencies: Tables and Charts. Wiley.

Sugimoto, T., 2007. Underlying mechanisms in size control of uniform nanoparticles. J. Colloid Interface Sci. 309, 106–118.

Tang, X.C., Pikal, M.J., Taylor, L.S., 2002. A spectroscopic investigation of hydrogen bond patterns in crystalline and amorphous phases in dihydropyridine calcium channel blockers. Pharm. Res. 19, 477–483.

Tantishaiyakul, V., Kaewnopparat, N., Ingkatawornwong, S., 1999. Properties of solid dispersions of piroxicam in polyvinylpyrrolidone. Int. J. Pharm. 181, 143–151.

Taylor, L.S., Zografi, G., 1997. Spectroscopic characterization of interactions between PVP and indomethacin in amorphous molecular dispersions. Pharm. Res. 14, 1691–1698.

Van Eerdenbrugh, B., Baird, J.A., Taylor, L.S., 2010. Crystallization tendency of active pharmaceutical ingredients following rapid solvent evaporation—classification and comparison with crystallization tendency from undercooled melts. J. Pharm. Sci. 99, 3826–3838.

Van Eerdenbrugh, B., Taylor, L.S., 2010. Small scale screening to determine the ability of different polymers to inhibit drug crystallization upon rapid solvent evaporation. Mol. Pharm. 7, 1328–1337.

Vasconcelos, T., Sarmento, B., Costa, P., 2007. Solid dispersions as strategy to improve oral bioavailability of poor water soluble drugs. Drug Discov. Today 12, 1068–1075.

Vrecer, F., Vrbinc, M., Meden, A., 2003. Characterization of piroxicam crystal modifications. Int. J. Pharm. 256, 3–15.

Wikström, H., Kakidas, C., Taylor, L.S., 2009. Determination of hydrate transition temperature using transformation kinetics obtained by Raman spectroscopy. J. Pharm. Biomed. Anal. 49, 247–252.

Wu, J.X., Yang, M., Berg F. v. d. Pajander, J., Rades, T., Rantanen, J., 2011. Influence of solvent evaporation rate and formulation factors on solid dispersion physical stability. Eur. J. Pharm. Sci. 44, 610–620.

Xia, D., Ouyang, M., Wu, J.X., Jiang, Y., Piao, H., Sun, S., Zheng, L., Rantanen, J., Cui, F., Yang, M., 2012. Polymer-mediated anti-solvent crystallization of nitrendipine: monodispersed spherical crystals and growth mechanism. Pharm. Res. 29, 158–169.

Zhou, G.X., Crocker, L., Xu, J., Tabora, J., Ge, Z., 2006. In-line measurement of a drug substance via near infrared spectroscopy to ensure a robust crystallization process. J. Pharm. Sci. 95, 2337–2347.